Intrinsic Limits of Charge Carrier Mobilities in Layered Halide Perovskites

Bruno Cucco, Joshua Leveillee, Viet-Anh Ha, Jacky Even, Mikaël Kepenekian, Feliciano Giustino, George Volonakis

▶ **To cite this version:**

Bruno Cucco, Joshua Leveillee, Viet-Anh Ha, Jacky Even, Mikaël Kepenekian, et al.. Intrinsic Limits of Charge Carrier Mobilities in Layered Halide Perovskites. PRX Energy, 2024, 3 (2), pp.023012. 10.1103/PRXEnergy.3.023012 . hal-04629904

HAL Id: hal-04629904
https://hal.science/hal-04629904v1

Submitted on 10 Sep 2024

HAL is a multi-disciplinary open access archive for the deposit and dissemination of scientific research documents, whether they are published or not. The documents may come from teaching and research institutions in France or abroad, or from public or private research centers.

L'archive ouverte pluridisciplinaire **HAL**, est destinée au dépôt et à la diffusion de documents scientifiques de niveau recherche, publiés ou non, émanant des établissements d'enseignement et de recherche français ou étrangers, des laboratoires publics ou privés.

Distributed under a Creative Commons Attribution 4.0 International License

Intrinsic Limits of Charge Carrier Mobilities in Layered Halide Perovskites

Bruno Cucco,[1,2,3] Joshua Leveillee,[2,3] Viet-Anh Ha,[2,3] Jacky Even,[4] Mikaël Kepenekian,[1] Feliciano Giustino,[2,3] and George Volonakis[1,*]

[1] *Univ Rennes, ENSCR, CNRS, ISCR (Institut des Sciences Chimiques de Rennes) – UMR 6226, F-35000 Rennes, France*

[2] *Oden Institute for Computational Engineering and Sciences, The University of Texas at Austin, Austin, Texas 78712, USA*

[3] *Department of Physics, The University of Texas at Austin, Austin, Texas 78712, USA*

[4] *Univ Rennes, INSA Rennes, CNRS, Institut FOTON – UMR 6082, F-35000 Rennes, France*

(Received 21 April 2024; revised 30 May 2024; accepted 7 June 2024; published 28 June 2024)

Layered halide perovskites have emerged as potential alternatives to three-dimensional (3D) halide perovskites due to their improved stability and larger material phase space, allowing fine tuning of structural, electronic, and optical properties. However, their charge carrier mobilities are significantly smaller than those of 3D halide perovskites, which has a considerable impact on their application in optoelectronic devices. Here, we employ state-of-the-art *ab initio* approaches to unveil the electron-phonon mechanisms responsible for the diminished transport properties of layered halide perovskites. Starting from a prototypical AMX_3 halide perovskite, we model the case of $n = 1$ and $n = 2$ layered structures and compare their electronic and transport properties to the 3D reference. The electronic and phononic properties are investigated within density functional theory (DFT) and density functional perturbation theory (DFPT), while transport properties are obtained via the *ab initio* Boltzmann transport equation. The vibrational modes contributing to charge carrier scattering are investigated and associated with polar-phonon scattering mechanisms arising from the long-range Fröhlich coupling and deformation-potential scattering processes. Our investigation reveals that the lower mobilities in layered systems primarily originate from the increased electronic density of states at the vicinity of the band edges, while the electron-phonon coupling strength remains similar. Such an increase is caused by the dimensionality reduction and the break in octahedra connectivity along the stacking direction. Our findings provide a fundamental understanding of the electron-phonon coupling mechanisms in layered perovskites and highlight the intrinsic limitations of the charge carrier transport in these materials.

DOI: 10.1103/PRXEnergy.3.023012

I. INTRODUCTION

Layered halide perovskites have emerged as a promising class of materials for optoelectronic applications due to their highly tunable physicochemical properties. These materials can be synthesized with different ordering along the stacking axis and number of inorganic layers n, which allows tuning of their optoelectronic properties via both dielectric and quantum confinement effects [1–3]. Their electronic properties can also be fine tuned by engineering the halogen and metal-site composition [4]. Different from many conventional lead-based halide perovskites, the layered perovskites can be highly stable in ambient conditions due to the possibility of introducing hydrophobic spacer cations, allowing significant improvements in their stability while preserving their photoactive properties [5–8].

As a state-of-the-art application, layered perovskites have been recently incorporated in two-dimensional (2D)/three-dimensional (3D) perovskite heterostructures for solar cells. These architectures are being currently investigated as a pathway to inherit the enhanced stability of layered systems while maintaining the high power conversion efficiencies of 3D perovskite solar cells [9–11]. Moreover, layered-perovskite-based light-emitting devices have been shown to allow the injection of large current values of several ampere per cm^2 [12] or exhibit high color purity and narrow emission, remarkably for blue phosphors, which is of interest for application in modern display technologies [13–15]. Despite these promising advances, the efficiency of layered

*Contact author: yorgos.volonakis@univ-rennes.fr

Published by the American Physical Society under the terms of the Creative Commons Attribution 4.0 International license. Further distribution of this work must maintain attribution to the author(s) and the published article's title, journal citation, and DOI.

perovskite-based optoelectronic devices is still severely hindered due to large electronic band gaps, strongly bounded excitons, and poor charge carrier mobilities at room temperature [16,17]. In particular, the charge carrier mobilities are shown to range from 0.36 $cm^2/V\,s$ to 8.7 $cm^2/V\,s$ [3,18] for layered systems, in contrast to 60.0 $cm^2/V\,s$ for the 3D perovskite $CH_3NH_3PbI_3$ [19]. As a result of the poor mobilities of layered systems, their application in many optoelectronic technologies is a major limiting factor toward highly efficient optoelectronic devices by comparison to other 2D quantum well-like semiconductors [20,21]. To date, various intrinsic or extrinsic mechanisms have been proposed to explain these reduced mobilities, such as large carrier effective masses [3], a high concentration of trap states that could act as scattering centers [22], and the presence of strongly bounded charge carriers (large exciton binding energies) that adversely affect charge carrier dissociation [17]. Yet, the fundamental atomic scale mechanisms underlying the measured low mobilities remain elusive, because a theoretical investigation of the transport properties, including accurate electron-phonon coupling in metal-halide layered materials, is still lacking.

In this work, we unveil the effect of dimensionality crossover from 3D to layered halide perovskites on transport properties. By employing a combination of density functional theory (DFT) and the state-of-the-art solution of the *ab initio* Boltzmann transport equation (*ai*BTE), we show that the measured decrease in the charge carrier mobilities of layered systems primarily originates from differences in charge carrier lifetimes. More importantly, by decomposing the different contributions to the charge carrier scattering rates, we demonstrate that the mobility of these systems is intrinsically limited by the significantly higher density of states (DOS) in the vicinity of the band edges due to the lower dimensionality. A symmetry analysis of the electron-phonon coupling reveals that polar-phonon scattering arising from the long-range Fröhlich coupling and nonpolar optical deformation-potential scattering are the main sources of charge carrier relaxation in layered perovskite materials.

II. RESULTS AND DISCUSSION

A. Structural models

To explore the structure-property relations in halide perovskites along dimension reduction, we start from the well-characterized 3D compound $CsPbBr_3$ in its orthorhombic phase [23,24]. We then build free-standing $n = 1$ (Cs_2PbBr_4) and $n = 2$ ($Cs_3Pb_2Br_7$) model layered perovskites. This choice of systems with inorganic cations allows us to focus on the effect of dimension reduction without being influenced by the choice made for large and small organic cations. We determine the appropriate ground-state (GS) structures within DFT by displacing the atomic coordinates in the unit cell following the imaginary phonon modes in each model structure. These are obtained via DFPT calculations. The set of atomic displacements can be written as

$$\Delta\chi_{\kappa\alpha p} = \left(\frac{M_0}{N_p M_\kappa}\right)^{1/2} \sum_{\mathbf{q}\nu} e^{i\mathbf{q}\cdot\mathbf{R}_p} e_{\kappa\alpha,\nu}(\mathbf{q}) z_{\mathbf{q}\nu}, \qquad (1)$$

where M_0 is the proton mass, M_κ is the mass of the κth ion, N_p is the number of unit cells in the Born–von Kármán (BvK) supercell, $\mathbf{q}$ is the crystal momentum of the lattice vibration, $e_{\kappa\alpha,\nu}(\mathbf{q})$ is the polarization of the acoustic wave corresponding to the wave vector $\mathbf{q}$ and mode ν, and $z_{\mathbf{q}\nu}$ are the normal-mode coordinates [25]. The GS structures of each material are shown in Fig. 1.

The relaxed GS structures of the $n = 1$, $n = 2$, and 3D models exhibit space groups $P4/mbm$ (no. 127), $P4bm$ (no. 100), and $Pnma$ (no. 62), respectively. The average Pb—Br bond lengths are nearly identical in all systems (3.04 Å, 3.04 Å, and 3.03 Å for 3D, $n = 1$, and $n = 2$, respectively), while the average in-plane tilting (angle Φ in Fig. 1) is 153.5° for $CsPbBr_3$, and 147.5° and 155.9° for $n = 1$ and $n = 2$ GS structures, respectively. The structural properties of the 3D compound are consistent with previously reported experimental and theoretical data for $CsPbBr_3$ [23,24]. In the same manner, the structural parameters obtained for the layered $n = 1$ system are in excellent agreement with the experimental data available in the literature. The in-plane tilting-angle deviations are of −2.2%, 0.06%, −0.47%, and −0.61% in relation to $(PEA)_2PbBr_4$ [PEA (bis(2-phenylethan-1-aminium))], (MPenDA)$PbBr_4$ [MpenDA (methyl-2-pentane-1,5-diaminium)], (ODA)$PbBr_4$ [ODA (octane-1,8-diaminium)], and (BDA)$PbBr_4$ [BDA (butyl-1,4-diaminium)], respectively [26,27]. The Pb—Br bond length deviation is of 0.98% in relation to $(PEA)_2PbBr_4$ [28]. The in-plane tilting angles are also consistent with the work of Stoumpos *et al.*, where $n = 1$ is shown to exhibit larger Pb—Br—Pb tiltings than $n = 2$ and 3D $MAPbI_3$ (where "MA" denotes methylammonium), which have similar tilting angles [29]. This analysis validates our model choice, as it confirms that we retain the essential characteristics of the octahedra network and its evolution going from 3D to layered systems.

B. Phonons and electrons

We then consider the phonon properties of our models obtained by DFPT calculations [Fig. 2(a)]. The highest phonon-frequency modes around 140–150 cm^{-1} for $CsPbBr_3$ are in agreement with previous calculations performed on the 3D cubic phase of $CsPbI_3$ and the orthorhombic phase of $MAPbI_3$, where these modes fall within the range 120–170 cm^{-1} [30]. Importantly, the phonon dispersions confirm the mechanical stability of our

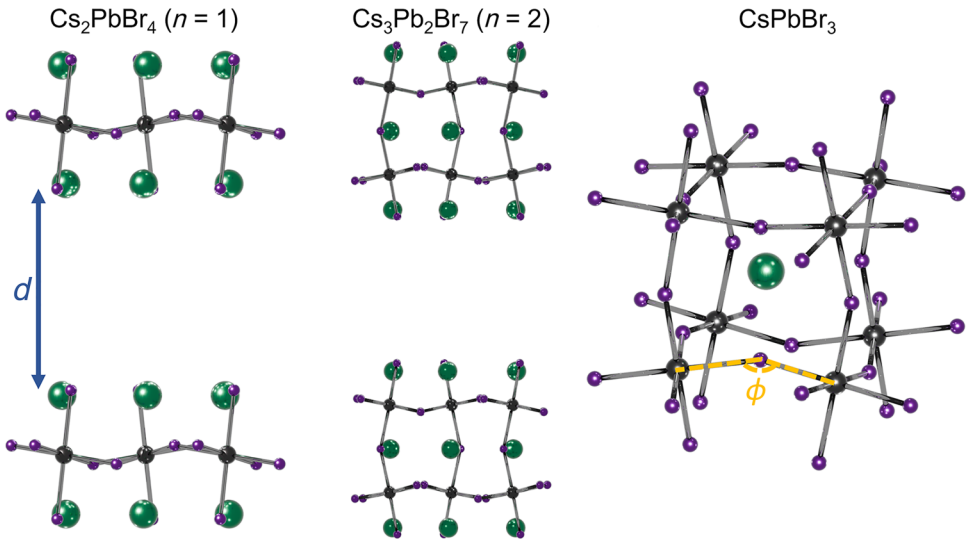

FIG. 1. Structural models of layered $n = 1$ and $n = 2$, and 3D halide perovskites. The interlayer distance d is defined as the shortest distance between halogens of different layers and is set to 35 Å to generate free-standing layers. The relaxed ground-state structures show structural parameters (Pb—Br bond length, in-plane tilting Φ) that are in excellent agreement with those of synthesized systems.

models, as the residual negative phonon modes are smaller than 0.01 cm^{-1}.

The electronic band structure of each system is shown in Fig. 2(b). The orthorhombic phase of $CsPbBr_3$ exhibits a direct band gap at the Γ point of the Brillouin zone, with a computed band gap of 1.04 eV and isotropic low hole ($0.25m_0$) and electron ($0.23m_0$) effective masses at the band edges. When going to the layered $n = 1$ model, the gap remains direct at Γ; however, the band gap increases to 1.86 eV, which constitutes a signature of the quantum and dielectric confinements [2,29]. The top valence band and bottom conduction band remain highly dispersive within the plane of the inorganic network and the hole ($0.40m_0$) and electron ($0.30m_0$) in-plane effective masses remain low and isotropic. With an increasing number of layers, the confinement is less pronounced and the band gap for $n = 2$, still direct, decreases to 1.44 eV, while the in-plane effective masses become $0.32m_0$ and $0.24m_0$ for holes and electrons, respectively. The similar in-plane effective masses are consistent with the similar structural parameters, such as the Pb—Br bond lengths and in-plane tilting angles.

Having obtained the electronic and phonon structures, we can move to calculation of the charge carrier mobilities. To provide insights on how the change in the effective mass between these systems affects the charge carrier mobilities, we first employ Drude's formula, $\mu = e\tau/m^*$, which leads to a mobility (μ) proportional to the carrier lifetime and inversely proportional to the charge carrier effective masses (m^*) [31,32]. By assuming similar carrier lifetimes and comparing the in-plane effective masses obtained within the parabolic approximation (Fig. 2), it would appear that the mobilities are not drastically affected by the changes in the effective masses that have originated from the dimensionality reduction. Thus, within these approximations, we conclude that by accounting for only changes in the effective masses, Drude's formula cannot explain the observed mobility drop of an order of magnitude when going from 3D to layered halide perovskites.

C. *Ab initio* charge carrier mobilities

Going beyond the Drude model, we proceed to compute charge carrier mobilities within an *ab initio* framework. To this aim, we express the charge carrier mobility tensor $\mu_{\alpha\beta}$ along arbitrary α and β directions [25] as follows:

$$\mu_{\alpha\beta} = \frac{1}{n_e \Omega} \sum_n \int \frac{d\mathbf{k}}{\Omega_{BZ}} v_{n\mathbf{k},\beta} \partial_{E\alpha} f_{n\mathbf{k}}. \tag{2}$$

Here, n_e is the carrier density, Ω and Ω_{BZ} are the volumes of the unit cell and Brillouin zone, respectively, $v_{n\mathbf{k},\beta}$ is the velocity of an electron with crystal momentum $\mathbf{k}$ at the band n along the β Cartesian direction, and $f_{n\mathbf{k}}$ is the out-of-equilibrium carrier distribution function. To evaluate the variation of the charge carrier distribution function in relation to the electric field along the α direction, $\partial_{E\alpha} f_{n\mathbf{k}}$, we solve the full *ai*BTE, given by

$$\begin{aligned}\partial_{E\alpha} f_{n\mathbf{k}} = e\frac{\partial f_{n\mathbf{k}}}{\partial \epsilon_{n\mathbf{k}}} v_{n\mathbf{k},\alpha}\tau_{n\mathbf{k}} + \frac{2\pi}{\hbar}\tau_{n\mathbf{k}} \sum_{m\nu} \int \frac{d\mathbf{q}}{\Omega_{BZ}} |g_{nm\nu}(\mathbf{k},\mathbf{q})|^2 \\ \times [(n_{\mathbf{q}\nu} + 1 - f^0_{n\mathbf{k}})\delta(\epsilon_{n\mathbf{k}} - \epsilon_{m\mathbf{k}+\mathbf{q}} + \hbar\omega_{\nu\mathbf{q}}) \\ + (n_{\mathbf{q}\nu} + f^0_{n\mathbf{k}})\delta(\epsilon_{n\mathbf{k}} - \epsilon_{m\mathbf{k}+\mathbf{q}} - \hbar\omega_{\nu\mathbf{q}})]\partial_{E\alpha} f_{m\mathbf{k}+\mathbf{q}},\end{aligned} \tag{3}$$

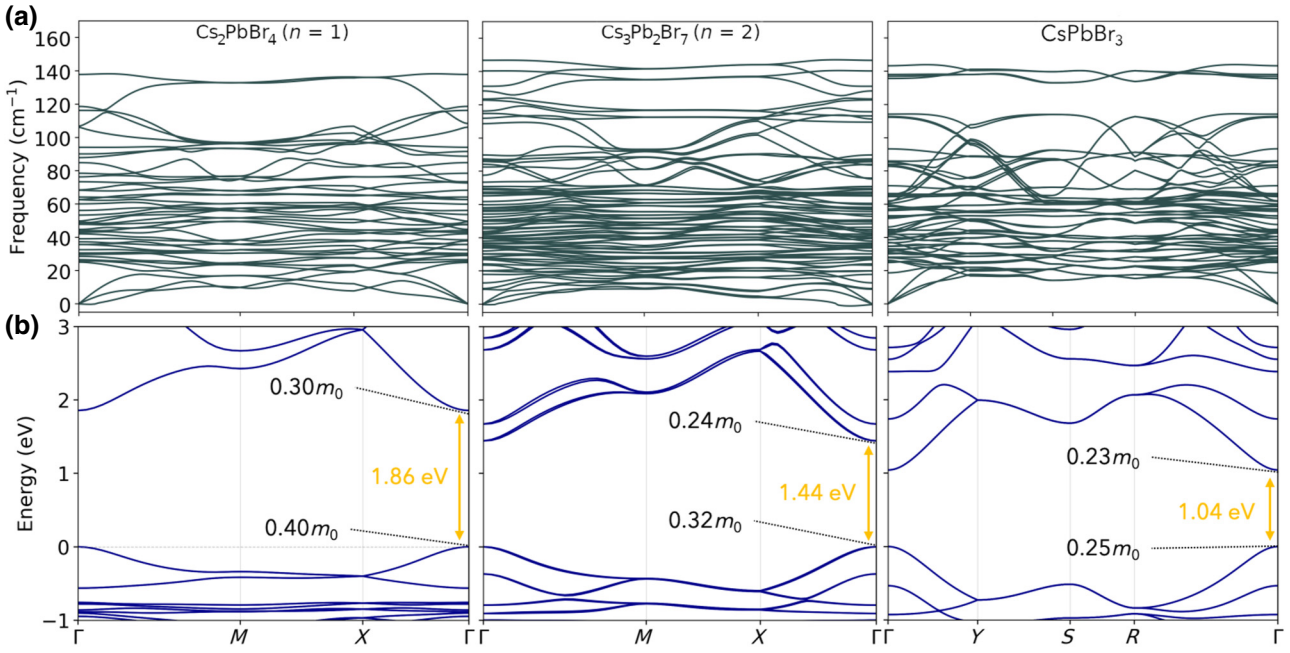

FIG. 2. Phononic and electronic structures: (a) the phonon dispersions and (b) the electronic band structure for the $n = 1$ and $n = 2$ layered halide perovskites ($Cs_{n+1}Pb_nBr_{3n+1}$) and the 3D $CsPbBr_3$. The fundamental band gaps and effective masses at band edges are provided.

where $g_{nm\nu}(\mathbf{k},\mathbf{q})$ are the electron-phonon (el-ph) matrix elements associated with the scattering of an electron from the initial state $n\mathbf{k}$ to the state $m\mathbf{k}+\mathbf{q}$ via a phonon with crystal momentum $\mathbf{q}$ in the branch ν [33]. The quantities $f^0_{n\mathbf{k}}$ and $n_{\mathbf{q}\nu}$ represent the equilibrium Fermi-Dirac and Bose-Einstein distributions, respectively. Finally, the lifetimes $\tau_{n\mathbf{k}}$ are obtained via the inversion of the scattering rates $\tau^{-1}_{n\mathbf{k}}$. Within the Fermi golden rule, this can be written as shown in Eq. (4). The phonon emission and absorption are being considered via the two terms within brackets [34–37]:

$$\tau^{-1}_{n\mathbf{k}} = \frac{2\pi}{\hbar}\sum_{m\nu}\int \frac{d\mathbf{q}}{\Omega_{BZ}}|g_{nm\nu}(\mathbf{k},\mathbf{q})|^2[(n_{\nu\mathbf{q}}+1-f^0_{m\mathbf{k}+\mathbf{q}}) \times \delta(\epsilon_{n\mathbf{k}}-\epsilon_{m\mathbf{k}+\mathbf{q}}-\omega_{\nu\mathbf{q}}) + (n_{\nu\mathbf{q}}+f^0_{m\mathbf{k}+\mathbf{q}}) \times \delta(\epsilon_{n\mathbf{k}}-\epsilon_{m\mathbf{k}+\mathbf{q}}+\omega_{\nu\mathbf{q}})]. \quad (4)$$

The *ab initio* calculated in-plane hole mobilities μ are shown in Fig. 3. The mobilities of all materials are decreasing with the increase of temperature, due to the increase of the charge carrier scattering by lattice vibrations, i.e., electron-phonon interactions. This is, by construction, the sole scattering mechanism considered in our calculations. Moreover, the in-plane mobility increases significantly when going from the layered to the 3D $CsPbBr_3$ structure, which reveals that dimensionality plays a critical role in the transport properties of perovskites. A similar phenomenon has been observed by Li *et al.* when studying 2D and bulk InSe [38] and also by Cheng *et al.* for a variety of 2D semiconductors [39]. The charge carrier mobility increases from 100 $cm^2/V\,s$ to 1000 $cm^2/V\,s$ when comparing 2D and bulk InSe. Conversely, carrier mobilities in classic III–V semiconductor quantum wells can reach very high values, due to quantum confinement that generates subbands and lifts the degeneracy of the valence band [20,40]. For lead bromide perovskites, at room temperature we predict hole mobilities of 4.3 $cm^2/V\,s$, 15.4 $cm^2/V\,s$, and 41.6 $cm^2/V\,s$ for the $n = 1$, $n = 2$, and 3D $CsPbBr_3$ structures, respectively. The obtained mobility for $CsPbBr_3$ is in excellent agreement with the 41 $cm^2/V\,s$ previously obtained by Poncé *et al.* for cubic $CsPbBr_3$, also within the same fully *ab initio* approach [30]. Other sets of calculations for $CsPbX_3$ (X = Cl, Br, I) employing different methodologies can also be found in the literature, such as Feynman polaron models [41], Bloch-Boltzmann theory [42], and numerical integration of the BTE using longitudinal-optical (LO) electron-phonon matrix elements within the Fröhlich model [43]. Additionally, the in-plane electron mobilities for the $n = 1$ and $n = 2$ layered systems are found to be 8.5 $cm^2/V\,s$ and 16.0 $cm^2/V\,s$, respectively (see Fig. S1 of the Supplemental Material [44]), revealing slightly larger mobilities for electrons, in agreement with the results of Poncé *et al.* for 3D halide perovskites [30]. It has been shown that the well-known DFT underestimation of the band-gap values can lead to a slight overestimation of mobilities of up to 15% [45]. The increase of the charge carrier mobilities as a function of the number of inorganic layers is consistent with previous works by Mitzi *et al.* [16] and Gélvez-Rueda

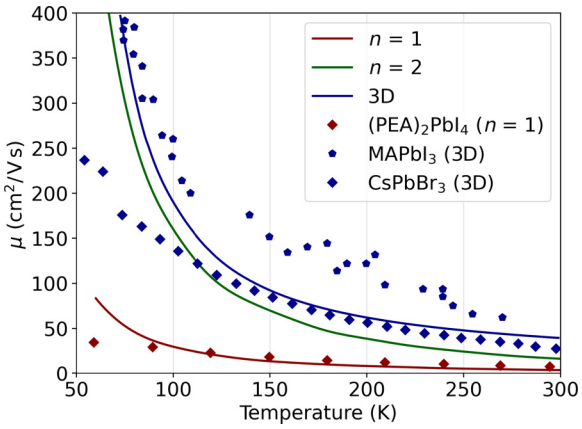

FIG. 3. Average in-plane hole mobilities. The calculations performed within the *ai*BTE approach for the $n = 1$, $n = 2$, and 3D systems are shown as solid lines. The experimental mobilities for the 3D structures $CsPbBr_3$ and $MAPbI_3$ have been extracted from Refs. [19,47], respectively. The mobility for $(PEA)_2PbI_4$ has been extracted from Ref. [18]. The experimental values correspond to the combined electron and hole mobilities.

et al. [3], reporting combined electron-hole mobilities. We also note that for the $n = 1$ and $n = 2$ systems, the mobilities have been calculated using the 2D form of the long-range Fröhlich coupling as proposed by Sio and Giustino [46]. In Fig. S2 of the Supplemental Material [44], we show a comparison between the hole mobilities employing the 2D and 3D forms of the long-range coupling. This highlights the importance of properly treating the Fröhlich coupling for the 2D compounds, due to the divergency of the el-ph matrix elements for small $\mathbf{q}$.

The scattering rates $\tau_{n\mathbf{k}}^{-1}$ related to the hole-carrier mobilities are shown in Fig. 4(a). At the valence-band top the scattering rates are considerably smaller, which indicates a large charge carrier lifetime. This is well established, as the carrier energies at band edges are below the threshold for LO phonon emission. The scattering rates are larger by more than an order of magnitude near the band edge for the layered $n = 1$ and $n = 2$ structures with respect to the 3D structure, which is consistent with the hole mobilities. This indicates that the mobility trend shown in Fig. 3 primarily originates from the different carrier lifetimes in each system.

Within time-dependent perturbation theory, the carrier lifetimes and scattering rates can be obtained from Fermi's golden rule [48]. In its simplest approximation, the scattering rate is directly proportional to the electron-phonon coupling strength $|g_{nm\nu}(\mathbf{k},\mathbf{q})|^2$ and the electronic DOS $D(\epsilon)$ at the vicinity of the band edges, i.e., $\tau^{-1} \propto |g_{nm\nu}(\mathbf{k},\mathbf{q})|^2 D(\epsilon)$. To unveil how the differences in the DOS of these systems contribute to the charge carrier scattering, in Fig. 4(b) we show the calculated electronic DOS near the valence-band edges for the three compounds. Within this narrow energy window, the DOS is more important for the layered systems than for the 3D $CsPbBr_3$. In conventional semiconductors, it can also be shown that as the number of octahedra layers n increases, the DOS of the layered systems decreases and converges to the 3D limit where $D(\epsilon) \propto \sqrt{\epsilon}$ [38]. This crossover of the electronic band structure from 2D to 3D can be understood by introducing 3D bulklike vertical masses. However, in perovskites, the electronic spacing of subbands and thus the connection between 2D and 3D DOS strongly depends on the local atomistic structure, including dangling bonds along the vertical axis [1]. The increased DOS calculated for the layered materials leads to an increased number of charge carriers being available to be scattered close to the band edges, which is the region being populated, and contributing to the charge carrier mobility at room temperature.

In order to disentangle the contributions coming from $|g_{nm\nu}(\mathbf{k},\mathbf{q})|^2$ and the DOS, in Fig. 4(c) we show the energy-averaged scattering rates [Eq. (5)] as a function of the electronic DOS, with both quantities evaluated at the characteristic energy $3K_bT/2$ from the band edge:

$$\tau_{\text{avg}}^{-1} = \frac{\sum_{nk} \tau_{nk}^{-1} \delta(\epsilon - \epsilon_{nk})}{\sum_{nk} \delta(\epsilon - \epsilon_{nk})}. \tag{5}$$

We have chosen to evaluate Eq. (5) at the energy $3K_bT/2$ as a reasonable descriptor for the carrier energy at room temperature, as previously shown by Poncé *et al.* [30] We show that there is a linear relation between τ_{avg}^{-1} and $D(\epsilon)$, which demonstrates that the electron-phonon coupling strength for the three systems is similar, as $\tau^{-1} \propto |g_{nm\nu}(\mathbf{k},\mathbf{q})|^2 D(\epsilon)$. These results show that the in-plane mobility of layered systems is intrinsically reduced by the more significant DOS in the vicinity of the band edges, while the electron-phonon coupling strength remains similar.

D. Spectral decomposition of the scattering rates

Having unveiled the origin of the short carrier lifetimes in the layered structures, we set out to further explore the different strongly coupled phonon modes. To this aim, we analyze the contribution of each phonon mode to the total scattering rate. This can be done by evaluating the variation of τ^{-1} in relation to the different phonon frequencies ω, i.e., $\partial\tau^{-1}/\partial\omega$. The spectral decomposition shown in Fig. 5 reveals that high-frequency optical modes dominate the scattering processes. In contrast, acoustic and low-frequency optical modes do not contribute significantly to the scattering rates. In this work, we neglect the effects of the quadrupole contributions to the electron-phonon matrix elements, which could increase the coupling to transversal out-of-plane acoustic (ZA), longitudinal acoustic (LA) and transversal in-plane acoustic (TA) phonon modes and

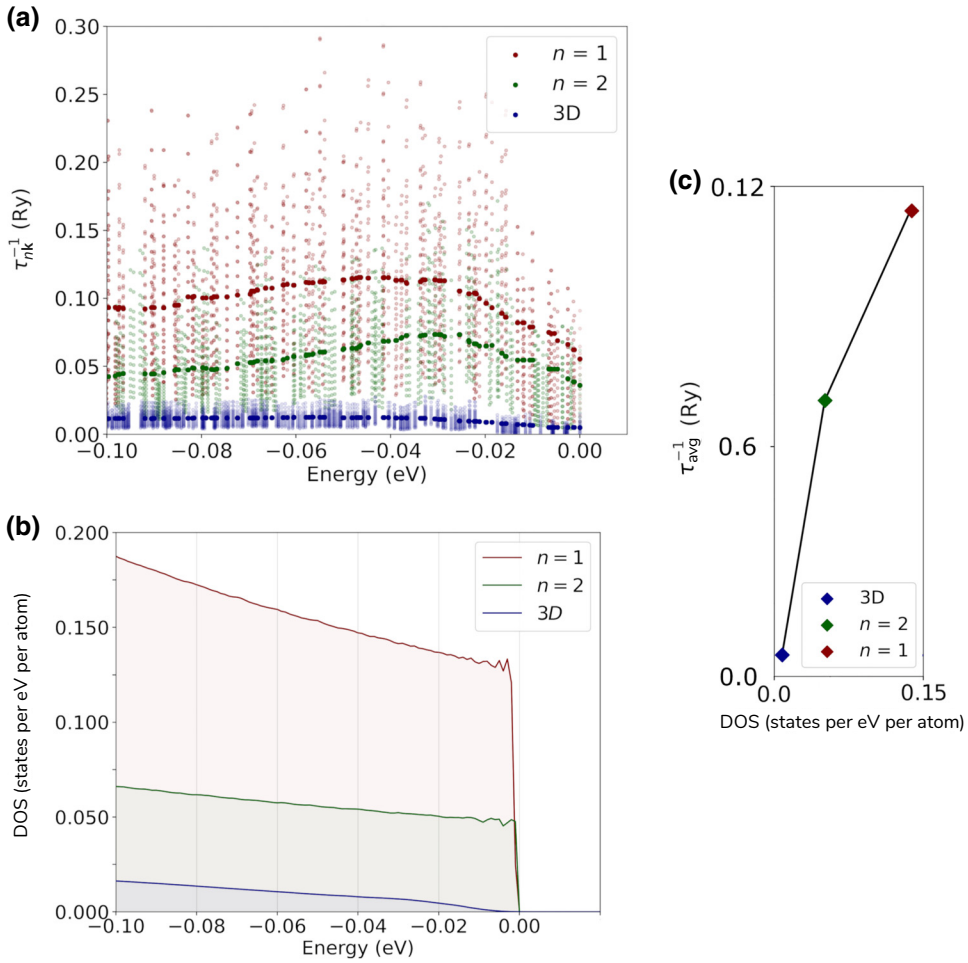

FIG. 4. Charge carrier scattering rates, the electronic density of states (DOS), and the electron-phonon coupling strength. (a) The scattering rates evaluated within the *ai*BTE approach. The points in dark colors represent the average scattering rates for each energy step. (b) The electronic DOS near the valence-band edge. The VBMs of the three systems are set to zero. (c) The energy-averaged scattering rate as a function of the electronic DOS.

further reduce the computed mobilities. In the case of $n = 1$, the primary source of charge carrier scattering is the LO phonons around 113 cm^{-1} and 121 cm^{-1}, which are related to Pb—Br stretching vibrations (peaks 1 and 2). Due to the absence of octahedra connectivity along the stacking direction, we observe a splitting of the scattering peak associated with Pb—Br stretching modes into in-plane (peak-1) and out-of-plane (peak-2) contributions. Our symmetry analysis at the Γ point for the peak-1 mode reveals that the Pb—Br stretching mode is related to the doubly degenerated E_u irreducible representation, which is infrared active and is also the vectorial representation of the D_{4h} point group in the x-y plane. Such a type of polar distortion of the lattice gives rise to an in-plane electric field that can scatter the charge carriers via the Fröhlich interaction. Analogously, the Pb—Br stretching mode of peak 2 is related to the A_{2u} representation, which is infrared active and is also the vectorial representation of the D_{4h} point group in the z direction.

For $n = 2$, the scattering rate is also dominated by LO phonons associated with a similar Pb—Br stretching mode contribution (peak 4) around 129 cm^{-1} and Pb—Br—Pb bending modes both in-plane and out-of-plane (peak 3) around 121 cm^{-1}. Our symmetry analysis at the Γ point for peak 4 shows that the stretching mode is associated with the A_1 representation, which is both infrared active and Raman active and is the vectorial representation of the C_{4v} point group in the z direction. Consequently, peak 4 observed for the $n = 2$ system has the same physical origin as for $n = 1$, which is related to Fröhlich coupling. However, the symmetry analysis for peak 3 shows that the Pb–Br–Pb bending modes are associated with the B_1 irreducible representation, which is Raman active but is not a vectorial representation of the C_{4v} point group. Therefore, these modes cannot give rise to a scattering electric field, as would be the case for a Fröhlich interaction. We associate the scattering mechanism of peak 3 with a nonpolar optical deformation-potential scattering. This type of

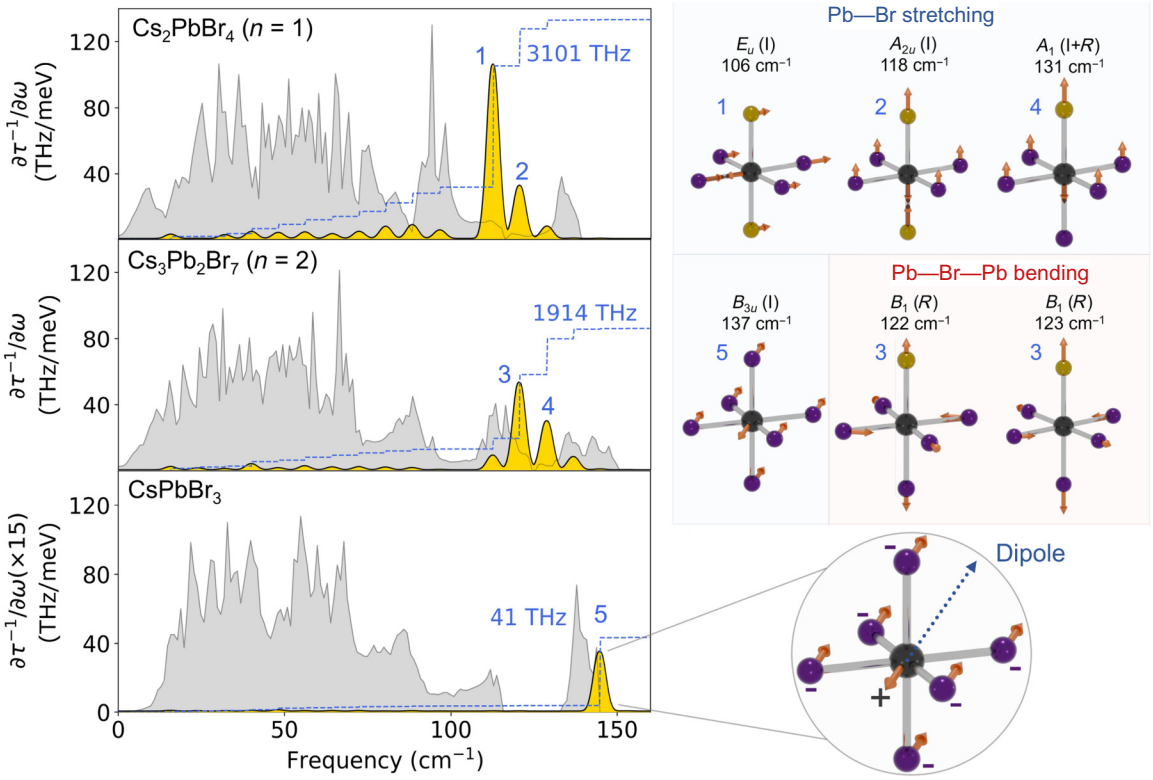

FIG. 5. The spectral decomposition of the contribution of phonons with energy $\hbar\omega$ to the scattering rates τ^{-1}. The spectral decompositions (yellow peaks) and vibrational-mode representations are shown for the $n = 1$ and $n = 2$ layered and 3D halide perovskites. The y axis of the 3D structure plot is multiplied by a factor of 15 for visibility. The phonon DOS is shown in gray. The cumulative integral (in terahertz) is shown in dotted blue. The atoms colored in gold represent the halogens that are not connected along the stacking direction. The gray boxes below each system indicate the space group and Γ point groups of each system. The labels R and I refer to Raman active and infrared active, respectively.

scattering can be understood by considering the intraband scattering limit at $q = 0$ for the electron-phonon matrix elements $g_{nm\nu}(\mathbf{k}, \mathbf{q})$, i.e., $g_{nn\nu}(\mathbf{k}, 0) = \langle u_{n\mathbf{k}}|\Delta_{0\nu} v_{\mathrm{SCF}}|u_{n\mathbf{k}}\rangle_{uc}$ (SCF stands for self-consistent field). In this expression, if the operator $\Delta_{0\nu} v_{\mathrm{SCF}}$ changes the symmetry of the Bloch state $|u_{n\mathbf{k}}\rangle$, this term will be zero due to the orthogonality of the Bloch states, leading to zero electron-phonon coupling. The only solutions leading to nonzero matrix elements are the ones where the operator preserves the symmetry of the initial Bloch state. For the $n = 2$ system, by analyzing the coupling between the phonon modes with irreducible representation B_1 with the charge carriers with irreducible representation E, we see that the transition matrices $\langle u_{n\mathbf{k}}|\Delta_{0\nu} v_{\mathrm{SCF}}|u_{n\mathbf{k}}\rangle_{uc}$ always contain the initial electronic state E, which satisfies the selection rule for the deformation-potential coupling [49]. Therefore, the nonpolar optical deformation-potential coupling between the Pb—Br—Pb bending modes with the charge carriers is allowed by symmetry and contributes to the charge carrier scattering.

Finally, the 3D system exhibits a sharp peak located at around 145 cm^{-1}, which also arises from the scattering via LO phonons and is related to a similar Pb—Br stretching mode as discussed for the layered systems. The symmetry analysis at the Γ point for peak 5 shows that the stretching mode is connected to the B_{3u} irreducible representation, which is infrared active and is also the vectorial representation of the D_{2h} point group. It is important to note that the nonpolar optical deformation-potential scattering processes predicted for the $n = 2$ system are not allowed by symmetry for either the $n = 1$ or the 3D system. This analysis is consistent with previous symmetry analysis performed by Even *et al.* for bulk cubic perovskites [50]. The spectral decomposition that we obtain for the bulk system is also consistent with previous calculations performed by Poncé *et al.* for $MAPbI_3$ [30] and experimental measurements by Pérez-Osorio *et al.* [51]. This analysis demonstrates that even if the dimensionality is reduced, the primary source of charge carrier relaxation in layered perovskites is still given by polar-phonon scattering mechanisms that arise from the long-range Fröhlich coupling, consistently with calculations for 3D systems such as AMX_3 halide perovskites [52] or $A_2MM'X_6$ halide double perovskites [53]. However, for the layered systems, we

describe additional scattering sources from phonon modes that originate from the absence of octahedra connectivity along the stacking direction. These processes are indeed allowed by symmetry even in the maximally symmetrized reference structures of 2D perovskites [20].

III. CONCLUSIONS

In conclusion, we have investigated the dimensionality crossover from 3D to layered halide perovskites and provided insights into the origin of the low charge carrier mobilities in the latter. Using state-of-the-art *ab initio* transport calculations, we have demonstrated that the decreased charge mobility observed in layered halide perovskites primarily originates from differences in the carrier lifetimes. By decoupling the different contributions to the charge carrier scattering rates, we have shown that an abrupt increase of the electronic DOS in the vicinity of the band edges for layered systems leads to increased charge scattering, and consequently poor charge transport. Conversely, the electron-phonon coupling strength remains similar between all systems. Furthermore, we employ electron-phonon symmetry analysis to demonstrate that, as for 3D perovskites, the primary source of charge carrier relaxation in layered perovskites is given by polar-phonon scattering mechanisms arising from the long-range Fröhlich coupling. However, due to the lack of octahedra connectivity along the stacking direction for layered materials, additional vibrational modes can contribute to the scattering rates. We also show that the $n = 2$ layered system can exhibit nonpolar optical deformation-potential scattering processes, which are not allowed by symmetry for either the 3D or the $n = 1$ system. Our findings provide a fundamental understanding of the electron-phonon coupling mechanisms governing the transport properties of layered metal-halide perovskites and demonstrate an intrinsic limitation of the charge carrier transport in these materials. We believe that due to these limitations, favoring layered perovskite materials with a large number of n layers would lead to higher device efficiencies in for example, 2D/3D heterostructures. Furthermore, the development of strategies to potentially reduce the electronic DOS in the vicinity of the band edges and/or damp the identified scattering modes via, e.g., composition engineering could potentially lead to higher performance. We are confident that this work can pave the way to the rational design of new layered perovskite-based devices and materials, exhibiting improved carrier lifetimes and more effective charge carrier separation.

IV. METHODS

A. Density functional theory

All the calculations within the DFT framework have been performed using the QUANTUM ESPRESSO suite [37,54]. The layered structures have been optimized with a 80-Ry cutoff for the plane-wave kinetic energy with a $4 \times 4 \times 1$ Brillouin-zone sampling, while a $4 \times 4 \times 4$ Brillouin-zone sampling has been employed for the 3D structure. The thresholds on forces and total energy during ionic minimization have been converged to 10^{-6} Ry/bohr and 10^{-11} Ry, respectively. During the optimizations, a 0.1-Kbar threshold has been employed for the pressure on the variable cell. A threshold of 10^{-11} Ry has been employed for the SCF steps. All the calculations for hole transport properties have been performed using a nonrelativistic norm-conserving PBE pseudopotential taken from the pseudo-dojo database [55,56], while the electron-transport properties have been evaluated taking spin-orbit interactions into account. The self-interaction error due to the DFT-PBE exchange-correlation functional has marginal effects on the computation of the electron-phonon matrix elements, as the charge carriers are delocalized [25]. Furthermore, although in perovskites the inclusion of spin-orbit coupling is fundamental to describe the complete valence-band manifold, in the vicinity of the band edges there are no significant changes in energy and band dispersion, as shown in Fig. S3 of the Supplemental Material [44]. The phonon calculations have been performed within the DFPT framework, as also implemented in QUANTUM ESPRESSO. A $4 \times 4 \times 4$ k-grid has been employed for the SCF, while the phonons have been solved in a $4 \times 4 \times 1$ q-grid for layered systems and a $2 \times 2 \times 2$ q-grid for the 3D system. A 10^{-17}-Ry threshold for phonon self-consistency has been employed.

B. *Ab initio* Boltzmann transport equation

The solution of the *ai*BTE has been performed with the EPW code [33–36,57]. For the calculation of layered systems, we have employed a $8 \times 8 \times 1$ and $4 \times 4 \times 1$ coarse k-grid and q-grid, respectively. These have been interpolated in fine grids of $60 \times 60 \times 1$ for both the k-grid and the q-grid. The interpolation of the electronic band structure has been performed using Wannier interpolation. For the Wannier interpolation of the valence and conduction band, we have started with only Pb orbitals as an initial set of projectors. The resulting orbitals lead to high-quality interpolation in the narrow energy range relevant to transport. The Wannier interpolated band structure and DFT, along with the corresponding MLWFs can be found in Fig. S4 of the Supplemental Material [44]. We note that a more complete set would be required to interpolate the complete valence- and conduction-band manifold. All states within 300 meV from the band edges have been included in the *ai*BTE calculation. For the 3D system, we have employed a $4 \times 4 \times 4$ and $2 \times 2 \times 2$ coarse k-grid and q-grid, respectively. These have been interpolated in fine grids of $50 \times 50 \times 40$ for both the k-grid and the q-grid. For the Wannier interpolation, Pb s orbitals and p orbitals

have been employed. All states within 300 meV from the band edges have been included in the *ai*BTE calculation.

The data that support the plots within this paper and other findings of this study are available from the corresponding authors upon request.

ACKNOWLEDGMENTS

We gratefully acknowledge the discussions with Professor V. Podzorov and Dr. V. Bruevich regarding intrinsic mobility measurements and the fruitful discussions with Dr. Hyungjun Lee and Professor S. Thébaud. The research leading to these results was supported by the Agence Nationale pour la Recherche through the CPJ program and the SURFIN project (Grant No. ANR-23-CE09-0001). This work was granted access to the High Performance Computing (HPC) resources of Trés Grand Centre de Calcul (TGCC) under the Allocation Grant No. 2022-A0130907682 made by Grand Equipement National de Calcul Intensif (GENCI). B.C., J.L., V.H., and F.G. are supported by the Robert A. Welch Foundation under Award No. F-2139-20230405 (calculations and manuscript preparation) and the Computational Materials Sciences Program funded by the U.S. Department of Energy, Office of Science, Basic Energy Sciences, under Award No. DE-SC0020129 (EPW software development). We acknowledge the Texas Advanced Computing Center (TACC) at The University of Texas at Austin for providing HPC resources, including the Lonestar6 and Frontera under Leadership Resource Allocation (LRAC) Award No. 2103991, that have contributed to the research results reported within this paper. This research has also used resources of the National Energy Research Scientific Computing Center, a DOE Office of Science User Facility supported by the Office of Science of the U.S. Department of Energy under Contract No. DE-AC02-05CH11231.

B.C. undertook the data curation. M.K., F.G. and G.V. conceptualized the project. B.C. carried out the investigations and wrote and edited the original draft. M.K. and G.V., and F.G. reviewed and edited the draft paper. M.K. and G.V. administered and validated the project and managed resources. F.G. and G.V. supervised the project and the funding acquisition. All the authors contributed to the formal analysis, the methodology and the editing of the paper.

The authors declare no competing interests.

[1] C. Katan, N. Mercier, and J. Even, Quantum and dielectric confinement effects in lower-dimensional hybrid perovskite semiconductors, Chem. Rev. **119**, 3140 (2019).

[2] L. Pedesseau, D. Sapori, B. Traore, R. Robles, H.-H. Fang, M. A. Loi, H. Tsai, W. Nie, J.-C. Blancon, A. Neukirch, S. Tretiak, A. D. Mohite, C. Katan, J. Even, and M. Kepenekian, Advances and promises of layered halide hybrid perovskite semiconductors, ACS Nano **10**, 9776 (2016).

[3] M. C. Gélvez-Rueda, E. M. Hutter, D. H. Cao, N. Renaud, C. C. Stoumpos, J. T. Hupp, T. J. Savenije, M. G. Kanatzidis, and F. C. Grozema, Interconversion between free charges and bound excitons in 2D hybrid lead halide perovskites, J. Phys. Chem. C **121**, 26566 (2017).

[4] R. Matheu, J. A. Vigil, E. J. Crace, and H. I. Karunadasa, The halogen chemistry of halide perovskites, Trends Chem. **4**, 206 (2022).

[5] I. C. Smith, E. T. Hoke, D. Solis-Ibarra, M. D. McGehee, and H. I. Karunadasa, A layered hybrid perovskite solar-cell absorber with enhanced moisture stability, Angew. Chem., Int. Ed. Engl. **53**, 11232 (2014).

[6] H. Tsai, W. Nie, J.-C. Blancon, C. C. Stoumpos, R. Asadpour, B. Harutyunyan, A. J. Neukirch, R. Verduzco, J. J. Crochet, S. Tretiak, *et al.*, High-efficiency two-dimensional Ruddlesden-Popper perovskite solar cells, Nature **536**, 312 (2016).

[7] M. D. Smith and H. I. Karunadasa, White-light emission from layered halide perovskites, Acc. Chem. Res. **51**, 619 (2018).

[8] Y. Zheng, T. Niu, X. Ran, J. Qiu, B. Li, Y. Xia, Y. Chen, and W. Huang, Unique characteristics of 2D Ruddlesden-Popper (2DRP) perovskite for future photovoltaic application, J. Mater. Chem. A **7**, 13860 (2019).

[9] J. Byeon, S. H. Cho, J. Jiang, J. Jang, C. Katan, J. Even, J. Xi, M. Choi, and Y. S. Lee, Structural isomer of fluorinated Ruddlesden-Popper perovskites toward efficient and stable 2D/3D perovskite solar cells, ACS Appl. Mater. Interfaces **15**, 27853 (2023).

[10] I. Metcalf, S. Sidhik, H. Zhang, A. Agrawal, J. Persaud, J. Hou, J. Even, and A. D. Mohite, Synergy of 3D and 2D perovskites for durable, efficient solar cells and beyond, Chem. Rev. **123**, 9565 (2023).

[11] S. Sidhik, *et al.*, Deterministic fabrication of 3D/2D perovskite bilayer stacks for durable and efficient solar cells, Science **377**, 1425 (2022).

[12] H. Tsai, W. Nie, J.-C. Blancon, C. C. Stoumpos, C. M. M. Soe, J. Yoo, J. Crochet, S. Tretiak, J. Even, A. Sadhanala, G. Azzellino, R. Brenes, P. M. Ajayan, V. Bulović, S. D. Stranks, R. H. Friend, M. G. Kanatzidis, and A. D. Mohite, Stable light-emitting diodes using phase-pure Ruddlesden-Popper layered perovskites, Adv. Mater. **30**, 1704217 (2018).

[13] M. D. Smith, B. A. Connor, and H. I. Karunadasa, Tuning the luminescence of layered halide perovskites, Chem. Rev. **119**, 3104 (2019).

[14] Q. Wang, J. Ren, X.-F. Peng, X.-X. Ji, and X.-H. Yang, Efficient sky-blue perovskite light-emitting devices based on ethylammonium bromide induced layered perovskites, ACS Appl. Mater. Interfaces **9**, 29901 (2017).

[15] N. Kawano, M. Koshimizu, Y. Sun, N. Yahaba, Y. Fujimoto, T. Yanagida, and K. Asai, Effects of organic moieties on luminescence properties of organic-inorganic layered perovskite-type compounds, J. Phys. Chem. C **118**, 9101 (2014).

[16] D. B. Mitzi, C. Feild, W. Harrison, and A. Guloy, Conducting tin halides with a layered organic-based perovskite structure, Nature **369**, 467 (1994).

[17] M. Kober-Czerny, S. G. Motti, P. Holzhey, B. Wenger, J. Lim, L. M. Herz, and H. J. Snaith, Excellent long-range charge-carrier mobility in 2D perovskites, Adv. Funct. Mater. **32**, 2203064 (2022).

[18] S. G. Motti, M. Kober-Czerny, M. Righetto, P. Holzhey, J. Smith, H. Kraus, H. J. Snaith, M. B. Johnston, and L. M. Herz, Exciton formation dynamics and band-like free charge-carrier transport in 2D metal halide perovskite semiconductors, Adv. Funct. Mater. **33**, 2300363 (2023).

[19] C. Q. Xia, J. Peng, S. Poncé, J. B. Patel, A. D. Wright, T. W. Crothers, M. Uller Rothmann, J. Borchert, R. L. Milot, H. Kraus, Q. Lin, F. Giustino, L. M. Herz, and M. B. Johnston, Limits to electrical mobility in lead-halide perovskite semiconductors, J. Phys. Chem. Lett. **12**, 3607 (2021).

[20] J.-C. Blancon, J. Even, C. C. Stoumpos, M. G. Kanatzidis, and A. D. Mohite, Semiconductor physics of organic-inorganic 2D halide perovskites, Nat. Nanotechnol. **15**, 969 (2020).

[21] R. L. Milot, R. J. Sutton, G. E. Eperon, A. A. Haghighirad, J. Martinez Hardigree, L. Miranda, H. J. Snaith, M. B. Johnston, and L. M. Herz, Charge-carrier dynamics in 2D hybrid metal-halide perovskites, Nano Lett. **16**, 7001 (2016).

[22] L. R. V. Buizza, T. W. Crothers, Z. Wang, J. B. Patel, R. L. Milot, H. J. Snaith, M. B. Johnston, and L. M. Herz, Charge-carrier dynamics, mobilities, and diffusion lengths of 2D–3D hybrid butylammonium–cesium–formamidinium lead halide perovskites, Adv. Funct. Mater. **29**, 1902656 (2019).

[23] G. Mannino, I. Deretzis, E. Smecca, A. La Magna, A. Alberti, D. Ceratti, and D. Cahen, Temperature-dependent optical band gap in $CsPbBr_3$, $MaPbBr_3$, and $FaPbBr_3$ single crystals, J. Phys. Chem. Lett. **11**, 2490 (2020).

[24] C. C. Stoumpos, C. D. Malliakas, J. A. Peters, Z. Liu, M. Sebastian, J. Im, T. C. Chasapis, A. C. Wibowo, D. Y. Chung, A. J. Freeman, B. W. Wessels, and M. G. Kanatzidis, Crystal growth of the perovskite semiconductor $CsPbBr_3$: A new material for high-energy radiation detection, Cryst. Growth Des. **13**, 2722 (2013).

[25] F. Giustino, Electron-phonon interactions from first principles, Rev. Mod. Phys. **89**, 015003 (2017).

[26] M. D. Smith, A. Jaffe, E. R. Dohner, A. M. Lindenberg, and H. I. Karunadasa, Structural origins of broadband emission from layered Pb–Br hybrid perovskites, Chem. Sci. **8**, 4497 (2017).

[27] D. Ghosh, A. J. Neukirch, and S. Tretiak, Optoelectronic properties of two-dimensional bromide perovskites: Influences of spacer cations, J. Phys. Chem. Lett. **11**, 2955 (2020).

[28] K. Shibuya, M. Koshimizu, F. Nishikido, H. Saito, and S. Kishimoto, Poly[bis(phenethy-ammonium) [dibromid oplumbate(II)]-di-μ-bromido]], Acta Cryst. E **65**, m1323 (2009).

[29] C. C. Stoumpos, D. H. Cao, D. J. Clark, J. Young, J. M. Rondinelli, J. I. Jang, J. T. Hupp, and M. G. Kanatzidis, Ruddlesden-Popper hybrid lead iodide perovskite 2D homologous semiconductors, Chem. Mater. **28**, 2852 (2016).

[30] S. Poncé, M. Schlipf, and F. Giustino, Origin of low carrier mobilities in halide perovskites, ACS Energy Lett. **4**, 456 (2019).

[31] P. Drude, Zur Elektronentheorie der Metalle, Ann. Phys. **306**, 566 (1900).

[32] P. Drude, Zur Elektronentheorie der Metalle; II. Teil. Galvanomagnetische und thermomagnetische Effecte, Ann. Phys. **308**, 369 (1900).

[33] S. Poncé, E. R. Margine, and F. Giustino, Towards predictive many-body calculations of phonon-limited carrier mobilities in semiconductors, Phys. Rev. B **97**, 121201(R) (2018).

[34] H. Lee, S. Poncé, K. Bushick, S. Hajinazar, J. Lafuente-Bartolome, J. Leveillee, C. Lian, J.-M. Lihm, F. Macheda, H. Mori, H. Paudyal, W. H. Sio, S. Tiwari, M. Zacharias, X. Zhang, N. Bonini, E. Kioupakis, E. R. Margine, and F. Giustino, Electron-phonon physics from first principles using the EPW code, npj Comput. Mater. **9**, 156 (2023).

[35] S. Poncé, E. Margine, C. Verdi, and F. Giustino, EPW: Electron-phonon coupling, transport and superconducting properties using maximally localized Wannier functions, Comput. Phys. Commun. **209**, 116 (2016).

[36] C. Verdi and F. Giustino, Frohlich electron-phonon vertex from first principles, Phys. Rev. Lett. **115**, 176401 (2015).

[37] P. Giannozzi, *et al.*, QUANTUM ESPRESSO: A modular and open-source software project for quantum simulations of materials, J. Phys. Condens. Matter. **21**, 395502 (2009).

[38] W. Li, S. Poncé, and F. Giustino, Dimensional crossover in the carrier mobility of two-dimensional semiconductors: The case of InSe, Nano Lett. **19**, 1774 (2019).

[39] L. Cheng, C. Zhang, and Y. Liu, Why two-dimensional semiconductors generally have low electron mobility, Phys. Rev. Lett. **125**, 177701 (2020).

[40] G. Bastard, *Wave Mechanics Applied to Semiconductor Heterostructures* (Wiley, New York, 1990).

[41] J. M. Frost, Calculating polaron mobility in halide perovskites, Phys. Rev. B **96**, 195202 (2017).

[42] A. Filippetti, A. Mattoni, C. Caddeo, M. I. Saba, and P. Delugas, Low electron-polar optical phonon scattering as a fundamental aspect of carrier mobility in methylammonium lead halide $CH_3NH_3PbI_3$ perovskites, Phys. Chem. Chem. Phys. **18**, 15352 (2016).

[43] Y. Kang and S. Han, Intrinsic carrier mobility of cesium lead halide perovskites, Phys. Rev. Appl. **10**, 044013 (2018).

[44] See the Supplemental Material at http://link.aps.org/supplemental/10.1103/PRXEnergy.3.023012 for the average in-plane electron mobilities, a comparison between 3D and 2D forms of the Fröhlich coupling term, the spin-orbit effect around the band edges for the valence bands, and a comparison between the Wannier interpolation and DFT.

[45] S. Poncé, F. Macheda, E. R. Margine, N. Marzari, N. Bonini, and F. Giustino, First-principles predictions of Hall and drift mobilities in semiconductors, Phys. Rev. Res. **3**, 043022 (2021).

[46] W. H. Sio and F. Giustino, Unified *ab initio* description of Fröhlich electron-phonon interactions in two-dimensional and three-dimensional materials, Phys. Rev. B **105**, 115414 (2022).

[47] V. Bruevich, L. Kasaei, S. Rangan, H. Hijazi, Z. Zhang, T. Emge, E. Y. Andrei, R. A. Bartynski, L. C. Feldman, and V. Podzorov, Intrinsic (trap-free) transistors based on epitaxial single-crystal perovskites, Adv. Mater. **34**, 2205055 (2022).

[48] G. Grimvall, *The Electron-Phonon Interaction in Metals* (University of California, U.S.A. and Canada, 1981).

[49] W. Ludwig and C. Falter, *Symmetries in Physics: Group Theory Applied to Physical Problems* (Springer Science & Business Media, 2012), Vol. 64, p. 256.

[50] J. Even, S. Paofai, P. Bourges, A. Letoublon, S. Cordier, O. Durand, and C. Katan, in *Physics, Simulation, and Photonic Engineering of Photovoltaic Devices V*, Vol. 9743, edited by A. Freundlich, L. Lombez, and M. Sugiyama, International Society for Optics and Photonics (SPIE, San Francisco, California, United States, 2016), p. 97430M.

[51] M. A. Pérez-Osorio, R. L. Milot, M. R. Filip, J. B. Patel, L. M. Herz, M. B. Johnston, and F. Giustino, Vibrational properties of the organic-inorganic halide perovskite $Ch_3Nh_3PbI_3$ from theory and experiment: Factor group analysis, first-principles calculations, and low-temperature infrared spectra, J. Phys. Chem. C **119**, 25703 (2015).

[52] M. Schlipf, S. Poncé, and F. Giustino, Carrier lifetimes and polaronic mass enhancement in the hybrid halide perovskite $Ch_3NH_3PbI_3$ from multiphonon Fröhlich coupling, Phys. Rev. Lett. **121**, 086402 (2018).

[53] J. Leveillee, G. Volonakis, and F. Giustino, Phonon-limited mobility and electron-phonon coupling in lead-free halide double perovskites, J. Phys. Chem. Lett. **12**, 4474 (2021).

[54] P. Giannozzi, *et al.*, Advanced capabilities for materials modelling with QUANTUM ESPRESSO, J. Phys. Condens. Matter **29**, 465901 (2017).

[55] http://www.pseudo-dojo.org

[56] M. van Setten, M. Giantomassi, E. Bousquet, M. Verstraete, D. Hamann, X. Gonze, and G.-M. Rignanese, The pseudodojo: Training and grading a 85 element optimized norm-conserving pseudopotential table, Comput. Phys. Commun. **226**, 39 (2018).

[57] F. Macheda and N. Bonini, Magnetotransport phenomena in p-doped diamond from first principles, Phys. Rev. B **98**, 201201(R) (2018).